Exp. Theo. NANOTECHNOLOGY 10 (2026) 453-470 https://doi.org/10.56053/10.2.453

Performance enhancement of unsaturated polyester using sustainable $CaCO_3$ nanoparticles: A multiscale characterization study

Eman Arif[1], *Rana Jamal*[2], *Mohammed RASHEED*[1,*]

[1]Production Engineering & Metallurgy College, University of Technology- Iraq, Baghdad, Iraq
[2]General Mechanics, Mechanical Engineering College, University of Technology- Iraq, Baghdad, Iraq
[*]) Email: rasheed.mohammed40@yahoo.com

Received 7/2/2026, *Received in revised form* 17/3/2026, *Accepted* 19/3/2026, *Published* 15/4/2026

In this study, unsaturated polyester (UPE) composites reinforced with oyster/shell-derived $CaCO_3$ nanoparticles (OSP) were fabricated with filler loadings of 1, 3, 5, 7, and 9 wt.% to evaluate their structural, mechanical, thermal, morphological, and antibacterial properties. Composite density increased from 1.20 g/cm³ (0%) to 1.30 g/cm³ (9%), confirming effective nanoparticle incorporation. XRD analysis showed enhanced calcite peak intensity with increasing OSP content, while crystallite size increased from 27.0 nm (1%) to 30.0 nm (7%). AFM results demonstrated a significant reduction in surface roughness, reaching 0.418 nm at 9 wt.%. FESEM images confirmed uniform dispersion at 5–7 wt.% and agglomeration at higher contents. Mechanical performance improved markedly, with optimal tensile (13.896 MPa), flexural (81.9 MPa), hardness (85.1 Shore D), impact strength (9.08 kJ/m²), and thermal conductivity (0.441 W/m·°C) observed at 5–7 wt.%. Antibacterial tests showed strong inhibition against *E. coli* and *S. aureus*, with complete *E. coli* elimination at 7 wt.%.

Keywords: UPE composites; Oyster/shell $CaCO_3$ NPs: Mechanical properties; XRD.

1. INTRODUCTION

Unsaturated polyester (UPE) resins are among the most widely used thermosetting polymers due to their favorable mechanical strength, chemical resistance, dimensional stability, and ease of processing [1]. However, their inherent brittleness and low thermal conductivity limit performance in demanding applications such as marine structures, automotive panels, and impact-resistant components [2]. To overcome these limitations, inorganic fillers are commonly incorporated into UPE matrices to enhance

stiffness, durability, and thermal behavior [3]. Calcium carbonate ($CaCO_3$) is used as filler material because it has a large specific surface area that can be improved by modifying its surface consequently containing low cost and good reinforcement of some polymers' properties. Newer studies have initiated biogenic $CaCO_3$ from oysters and marine shells as a possible environmentally friendly alternative source in comparison with mined type filler. The dominance is between aragonite and calcite phases including natural hierarchical micro- (211) besides nano-structures. Seafood waste abundance and the preferable physicochemical properties were suitable for the preparation of $CaCO_3$ NPs from an oyster/shell precursor (OSP) as a cheaper, low-environmental load reinforcement in polymer composites. The UPE, OSP use to enhance the mechanical properties, surface morphology, thermal behavior of WBEs plastic wastes give UPE and OSP use to enhance the mechanical properties, surface morphology, thermal behavior of WBEs plastic wastes besides giving significant contribution in waste valorization and circular material concept. However, the structure property knowledges of UPE composite are almost unavailable with regards to effect by loading OSP nanoparticle [8]. Up to now, most researches only concentrate on additives of micron size or single properties of the product without testing for crystallography response, micro-strains, particle distributions and surface morphologies [9]. Therefore, the effective loading of nanoparticulate on certain properties such as density, crystallinity, William-son–Hall parameters and thermal conductivity is not known [10]. In this work, UPE/OSP composites with various OSP contents of 1, 3, 5, 7 and 9 wt. %). FE-SEM testing for as synthesized products and XRD WH AFM thermal and density mechanical properties crystal structure surface morphology were applied. To the best of our knowledge, he is the first to report on the determination of optimum level of OSP for improvement in composites behavior and contribute towards guidance for the high-performance sustainable polymer composite designed for engineering applications.

2. MATERIALS AND METHODS

2.1. Materials

Commercial unsaturated polyester (UPE) resin with methyl ethyl ketone peroxide (MEKP) as the curing agent and cobalt naphthenate as the accelerator were procured from a certified supplier. Waste oyster/shell materials were collected from local seafood processing sources. All chemicals used—including ethanol, acetone, and deionized water—were of analytical grade and used without further purification.

2.2. Preparation of Oyster/Shell $CaCO_3$ nanoparticles (OSP)

2.2.1. Cleaning and Pre-treatment

The collected oyster/shell waste is washed thoroughly with tap water to remove organic residues, followed by rinsing with deionized water. The shells were dried in an oven at 105 °C for 24 h to eliminate moisture.

2.2.2. Grinding and Pulverization

The dried shells were initially crushed using a mechanical grinder and subsequently milled into fine powder using a planetary ball mill operating at 300 rpm for 6–8 h. The powder is sieved through a 100-mesh sieve to remove coarse particles.

2.2.3. Calcination and Nanoparticle Formation

To ensure removal of residual organics and enhance crystallinity, the sieved powder is calcined at 800 °C for 3 h in a muffle furnace. The calcined material is subjected to secondary high-energy ball milling

for 12 h to obtain nanoscale $CaCO_3$ particles. Particle size confirmation is performed through XRD and AFM analyses.

2.3. Fabrication of UPE/OSP nanocomposites
2.3.1. Mixing Procedure

OSP nanoparticles were incorporated into UPE at loadings of 0, 1, 3, 5, 7, and 9 wt.%. The required amount of OSP is weighed and dispersed into the UPE resin using a magnetic stirrer for 30 min, followed by ultrasonication for 20 min to minimize agglomeration and ensure uniform distribution.

2.3.2. Curing

After achieving homogeneous dispersion, 1 wt.% cobalt naphthenate and 1–2 wt.% MEKP were added as accelerator and catalyst, respectively, and mixed gently to avoid entrapped air bubbles. The mixture is poured into pre-cleaned silicone molds and allowed to cure at room temperature for 24 h post-curing is carried out in an oven at 60 °C for 3 h to ensure full crosslinking.

3. RELEVANT CHEMICAL REACTION EQUATIONS
3.1. Formation of unsaturated polyester resin (UPE)

UPE is synthesized by polycondensation between a diacid/anhydride and a diol [11].
Main Reaction (Polycondensation)

$$Maleic\ anhydride + Propylene\ glycol \xrightarrow{\Delta} Unsaturated\ polyester + H2O \quad (1)$$

Expanded form:

$$n(HO–CH_2–CH(CH_3)–OH)+n(C_2H_2(CO)_2O)\rightarrow[-O–CH_2–CH(CH_3)–O–CO–CH=CH–CO^-]n+n(H_2O) \quad (2)$$

This produces an unsaturated polyester backbone containing carbon–carbon double bonds.

3.2. Crosslinking of UPE with styrene (curing reaction)

During curing, styrene acts as a reactive diluent and crosslinking monomer [12]. Free-Radical Crosslinking Reaction:
Initiation (from MEKP initiator):

$$RO–O\bullet \rightarrow R\bullet+O\bullet \quad (3)$$

Propagation:

$$R\bullet+CH_2=CHPh \rightarrow R–CH_2–CHPh\bullet \quad (4)$$

Crosslinking with UPE backbone:

$$UPE–CH=CH–+\bullet CH_2–CHPh \rightarrow UPE–CH–CH–CH_2–CHPh\bullet \quad (5)$$

Final polymer network:

$$UPE + Styrene \xrightarrow{Free\ radicals} 3D\ Crosslinked\ Polyester\ Network \quad (6)$$

This reaction explains the rigid thermoset structure.

3.3. *$CaCO_3$ nanoparticle structure (from oyster shell)*

Oyster-shell $CaCO_3$ is primarily calcite, with the formula: $CaCO_3(s)$. Dissociation (surface interaction in the polymer):

$$CaCO_3 \rightleftharpoons Ca^{2+}+CO_3^{2-} \quad (7)$$

This partial dissociation improves surface reactivity and interfacial bonding with polyester chains.

3.4. Interactions between UPE matrix and $CaCO_3$ nanoparticles

Electrostatic / polar interactions [13]:

$$UPE–COOH+Ca^{2+}\rightarrow UPE–COO{-}Ca^{2+} \quad (8)$$

Hydrogen-bonding interactions: Hydrogen bonds form between hydroxyl groups on UPE and the oxygen atoms of the carbonate ion (CO_3^{2-}). Although weaker than ionic bonding, hydrogen bonding enhances compatibility and dispersion of $CaCO_3$ within the polymer matrix. These bonds help reduce microvoids, promoting higher mechanical integrity and increased density [14]

$$UPE–OH\cdots O=C\text{-}O\ (CaCO_3) \quad (9)$$

These interactions enhance: mechanical strength, stiffness, load transfer and reduction of microvoids

3.5. Antibacterial mechanism of UPE/OSP nanocomposites

The antibacterial activity of the UPE/OSP nanocomposites originates from several interconnected chemical and physical processes associated with the presence of $CaCO_3$ nanoparticles. One of the primary mechanisms involves the partial dissolution of $CaCO_3$ in the mildly acidic microenvironment produced by bacterial metabolism. Many bacteria release metabolic acids, such as acetic and lactic acid, lowering the local pH at the cell–material interface. In such conditions, $CaCO_3$ nanoparticles undergo proton-assisted dissolution according to [15]:

$$CaCO_3+2H^+\rightarrow Ca^{2+}+HCO_3{-}+H_2O \quad (10)$$

This reaction releases calcium ions into the medium, disturbing bacterial ionic regulation, altering osmotic pressure, and weakening cellular membranes. In addition, bicarbonate ions formed in solution can undergo secondary dissociation reactions, serving as a buffering system that elevates local pH levels [16]:

$$HCO_3^-\rightleftharpoons CO_3^{2-}+H^+ \quad (11)$$
$$HCO_3^-+H^+\rightarrow H_2CO_3\rightarrow H_2O+CO_2\uparrow \quad (12)$$

The overall rise in pH disrupts enzymatic processes and inhibits energy metabolism in both Gram-positive and Gram-negative bacteria, particularly affecting *E. coli*, which is sensitive to even small pH elevations. Beyond dissolution, $CaCO_3$ nanoparticles actively participate in electrostatic interactions with bacterial cell walls. Bacterial membranes, rich in negatively charged groups such as carboxylates and phosphates, are attracted to the partially positively charged Ca^{2+} sites on the nanoparticle surface. This leads to strong local interactions described by:

$$Ca^{2+}{}_{surface}+LPS{-}_{bacteria}\rightarrow Ca–LPS\ complex \quad (13)$$

These interactions compress, destabilize, and permeabilize the cell envelope, eventually initiating leakage of intracellular constituents. For Gram-positive bacteria, such as *S. aureus*, similar interactions occur between Ca^{2+} ions and the negatively charged teichoic acids in the thick peptidoglycan layer:

$$Teichoic\ acid^-+Ca^{2+}\rightarrow Teichoic\ acid–Ca^+ \quad (14)$$

The result is a localized collapse or rigidification of the cell wall that compromises membrane fluidity and hinders normal cellular function. A further antibacterial mechanism arises from reactive oxygen species (ROS) generation, promoted by nanoparticle surfaces and trace metallic impurities naturally present in biogenic $CaCO_3$. Although $CaCO_3$ is not a major ROS source, nano-sized particles enhance electron transfer reactions in aqueous and oxygen-rich environments. This leads to the stepwise formation of highly reactive oxidative species:

$$O_2+e^-\rightarrow O_2^{\bullet-} \quad (15)$$
$$2O_2^{\bullet-}+2H^+\rightarrow H_2O_2+O_2 \quad (16)$$
$$H_2O_2+e^-\rightarrow \bullet OH+OH^- \quad (17)$$

Hydroxyl radicals (•OH) and hydrogen peroxide (H_2O_2) attack membrane lipids, oxidize proteins, and damage bacterial DNA. Oxidative stress eventually overwhelms the cell's defense mechanisms, leading to metabolic collapse and cell death. The combination of ROS attack and Ca^{2+}-induced ionic imbalance makes the composite surface increasingly hostile to microbial survival. A complementary antibacterial pathway is nutrient adsorption. $CaCO_3$ nanoparticles possess a highly reactive surface capable of adsorbing amino acids, enzymes, co-factors, and cell wall fragments released by bacteria. This process follows simple adsorption behavior, represented as [17]:

$$\text{Biomolecule (B)}+CaCO_3\rightarrow B\text{–}CaCO_3\text{(adsorbed)} \quad (18)$$

By immobilizing essential biomolecules, the nanoparticles deprive bacteria of nutrients required for growth and proliferation. The loss of enzymes and metabolic intermediates inhibits protein synthesis and reduces ATP availability, contributing to bacteriostatic or bactericidal effects. Finally, structural characterization (AFM and FESEM) shows that increased $CaCO_3$ loading significantly modifies the surface morphology of UPE, reducing roughness and limiting bacterial adhesion. While not a chemical reaction, this mechanism plays a crucial role in preventing bacteria from establishing stable contact points necessary for colonization and biofilm formation. In Gram-negative bacteria, Ca^{2+} cross-linking reactions can also reinforce the antibacterial effect by bridging adjacent carboxylate groups in the outer membrane:

$$R\text{–}COO^-+Ca^{2+}+OOC\text{–}R\rightarrow R\text{–}COO\text{–}Ca\text{–}OOC\text{–}R \quad (19)$$

This cross-linking reduces membrane flexibility, increases permeability, and accelerates cell lysis under environmental stress. Taken together, these chemical and physical pathways—$CaCO_3$ dissolution, Ca^{2+} release, pH modulation, ROS formation, nutrient adsorption, electrostatic interactions, cross-linking of membrane components, and reduced adhesion due to modified surface topography—act synergistically to inhibit bacterial growth on UPE/OSP composites. This explains why pure UPE, which lacks all these mechanisms, shows no antibacterial response, while $CaCO_3$-reinforced composites, especially around the optimized 5 wt.% loading, display measurable inhibition zones and strong bactericidal effects in ADM and SPM assays.

3.6. Characterization

A comprehensive set of structural, morphological, mechanical, thermal, and antibacterial characterization techniques is employed to evaluate the UPE/OSP composites. Density is measured in accordance with ASTM D792 using an electronic analytical balance (Shimadzu AUW220D, Japan), with values averaged from three measurements. X-ray diffraction (XRD) analysis is carried out using a PANalytical X'Pert PRO diffractometer with Cu–Kα radiation (λ = 0.15406 nm) over a 2θ range of 10–80°, and crystallite size and microstrain were determined using the Debye–Scherrer approach.

Surface morphology is examined by atomic force microscopy (AFM, NT-MDT NTEGRA Prima) in tapping mode, while particle dispersion and interfacial bonding were analyzed using field-emission scanning electron microscopy (FESEM, ZEISS Sigma 300 VP) after cryo-fracturing and gold sputtering. Mechanical properties were evaluated following ASTM standards, including tensile (ASTM D638), flexural (ASTM D790), impact (ASTM D256), and hardness (ASTM D2240) tests. Thermal conductivity is measured using a Hot Disk TPS 2500S analyzer. Antibacterial activity against *Escherichia coli* and *Staphylococcus aureus* is assessed using the Agar Diffusion and Spread Plate methods. All tests were performed in triplicate, and results were reported as mean ± standard deviation.

4. RESULTS AND DISCUSSION

4.1. Density

The density of composites (ρ_c) is typically calculated using the rule of mixtures [18]:

$$\rho_c = \frac{W_f + W_m}{\frac{W_f}{\rho_f} + \frac{W_m}{\rho_m}} \tag{20}$$

where: W_f = weight fraction of filler ($CaCO_3$), W_m= weight fraction of matrix (polyester), ρ_f= density of filler (≈ 2.70 g/cm³ for $CaCO_3$), and ρ_m= density of matrix (≈ 1.20 g/cm³ for polyester). Since only the filler concentration in wt.% is varied, the weight fractions can be written as [19]:

$$W_f = \frac{C}{100}, W_m = 1 - W_f \tag{21}$$

where C is the filler concentration (wt.%) [20].

Thus, $$\rho_c = \frac{1}{\frac{W_f}{\rho_f} + \frac{W_m}{\rho_m}} \tag{22}$$

Table 1 summarizes the density of neat UPE and UPE composites reinforced with oyster/shell $CaCO_3$ nanoparticles (OSP). A consistent increase in density is observed with increasing filler content, rising from 1.20 g/cm³ for pure UPE to 1.30 g/cm³ at 9 wt.% OSP. The baseline density reflects the organic nature of the polymer matrix. Addition of 1 wt.% OSP increases density to 1.22 g/cm³, indicating effective nanoparticle incorporation without void formation. Further increases at 3 and 5 wt.% OSP (1.24 and 1.26 g/cm³) suggest improved packing efficiency as nanoparticles occupy intermolecular free volume. Higher loadings (7–9 wt.%) yield more compact, inorganic-rich structures. Overall, the monotonic density increase confirms good filler–matrix compatibility and enhanced structural integrity of the composites.

Table 1 Density of UPE/OSP composites at different filler concentrations.

UPE/OSP Concentration (%)	Density
0	1.20
1	1.22
3	1.24
5	1.26
7	1.28
9	1.30

4.2. XRD analysis

Figure 3 shows the XRD patterns of pure UPE and UPE composites reinforced with 1–9 wt.% oyster/shell $CaCO_3$ (OSP). Neat UPE exhibits a broad amorphous halo centered at $2\theta \approx 18–22°$, confirming the absence of long-range crystalline order. With OSP incorporation, sharp diffraction peaks appear at $2\theta \approx 29.4°$, 36.0°, 39.4°, 43.1°, and 47.5°, corresponding to the (104), (110), (113), (202), and (018) planes of calcite $CaCO_3$. The calculated structural parameters derived from these peaks are summarized in Table 2. The interplanar spacing is determined using Bragg's law, $d=\lambda/(2\sin\theta)$ [21], while the crystallite size is estimated by the Debye–Scherrer equation, $D=K\lambda/(\beta\cos\theta)$. Microstrain and dislocation density were evaluated using $\varepsilon=\beta/(4\tan\theta)$ and $\delta=1/D^2$, respectively [22, 23]. The calcite unit-cell volume is calculated as $V=3/2a^2c$ [24, 25]. As detailed in Table 2, increasing OSP content leads to peak sharpening, increased crystallite size, and reduced microstrain, confirming enhanced crystallinity without formation of secondary phases.

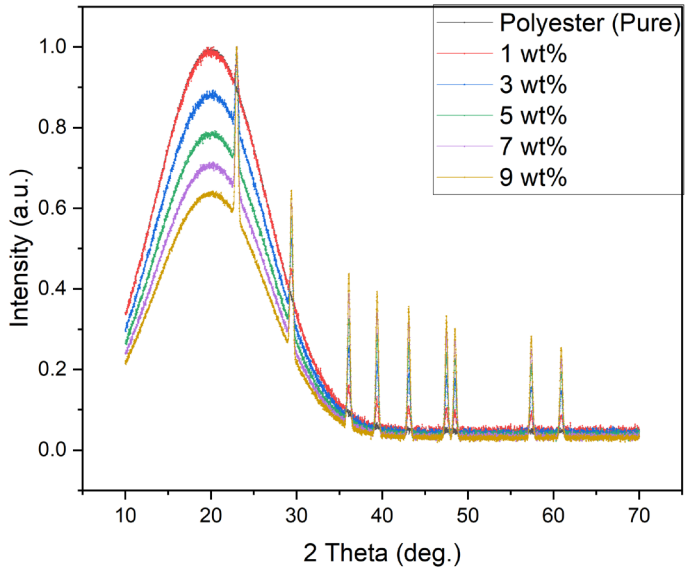

Figure 3 XRD values of Oyster/Shell $CaCO_3$ Nanoparticles in Polyester composites.

Table 3 XRD parameters for UPE/OSP composites with different concentrations 1, 3, 5, 7, and 9 wt.%

Samples (OSP)	2θ (°)	FWHM	(hkl)	d-Spacing (A°)	V (Å^3)	D_{cs} (nm)	(ε)×10^{-12} (m)	δ ×10^{-12} (m)
1 wt.%	29.40	0.280	(104)	3.036	367.88	29.3	4.657	11.622
	36.00	0.300	(110)	2.493		27.8	4.029	12.899
	39.40	0.310	(113)	2.285		27.2	3.778	13.497
	43.10	0.330	(202)	2.097		25.9	3.646	14.927
	47.50	0.350	(018)	1.913		24.8	3.471	16.262
Ave.	—	0.314	—	2.365	—	27.0	3.916	13.841
3 wt.%	29.40	0.270	(104)	3.036	368.34	30.4	4.491	10.807
	36.00	0.290	(110)	2.493		28.8	3.894	12.053
	39.40	0.300	(113)	2.285		28.1	3.656	12.640
	43.10	0.320	(202)	2.097		26.7	3.536	14.036
	47.50	0.340	(018)	1.913		25.5	3.372	15.346
Ave.	—	0.304	—	2.365	—	27.9	3.790	12.976
5 wt.%	29.40	0.260	(104)	3.036	369.12	31.6	4.326	10.023
	36.00	0.280	(110)	2.493		29.8	3.760	11.254
	39.40	0.290	(113)	2.285		29.0	3.531	11.891
	43.10	0.310	(202)	2.097		27.6	3.419	13.113
	47.50	0.330	(018)	1.913		26.4	3.262	14.355
Ave.	ave	0.294	—	2.365	367.88	28.9	3.660	12.927
7 wt.%	29.40	0.250	(104)	3.036	367.84	32.9	4.161	9.249
	36.00	0.270	(110)	2.493		31.0	3.626	10.398
	39.40	0.280	(113)	2.285		30.2	3.407	10.954
	43.10	0.300	(202)	2.097		28.7	3.316	12.159
	47.50	0.320	(018)	1.913		27.4	3.073	13.340
Ave.	ave	0.284	—	2.365		30.0	3.517	11.620
9 wt.%	29.40	0.260	(104)	3.036	370.36	31.6	4.326	10.023
	36.00	0.290	(110)	2.493		28.8	3.894	12.053
	39.40	0.300	(113)	2.285		28.1	3.656	12.640
	43.10	0.320	(202)	2.097		26.7	3.536	14.036
	47.50	0.340	(018)	1.913		25.5	3.372	15.346
Ave		0.302	—	2.365		28.1	3.757	12.820

4.3. AFM analysis

Figure 5 shows the 2D and 3D AFM images of UPE/OSP composites with 0, 1, 5, and 9 wt.% OSP. Pure UPE exhibits the highest surface roughness, with Ra = 0.963 nm and Rq = 0.517 nm, indicating a heterogeneous surface. Upon adding 1 wt.% OSP, roughness decreases to Ra = 0.715 nm and Rq = 0.202 nm, reflecting effective nanoparticle dispersion. Further reductions are observed at 5 wt.% (Ra = 0.643 nm, Rq = 0.140 nm) and 9 wt.% OSP (Ra = 0.418 nm, Rq = 0.113 nm), confirming progressive surface smoothing and enhanced surface uniformity due to efficient micro-void filling by OSP nanoparticles [26,27].

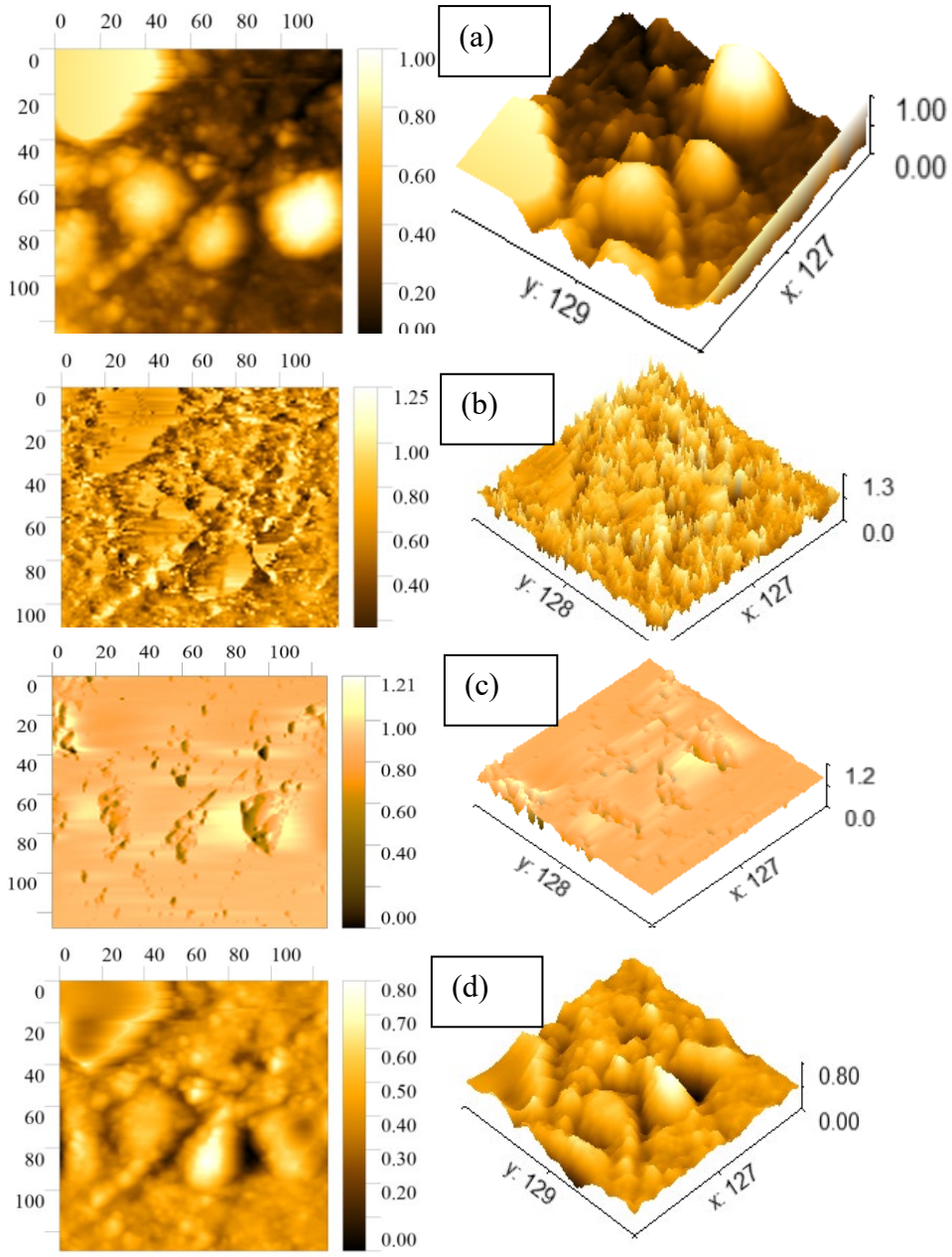

Figure 5 AFM 2D and 3D surface morphology of UPE/OSP composites at (a) 0%, (b) 1%, (c) 5%, and (d) 9 wt.% nanofiller loadings

4.4. FESEM analysis

Figure 6 presents FESEM micrographs of UPE/OSP composites at 0, 1, 5, and 9 wt.% OSP, captured at 110,000× magnification with a 500 nm scale bar. Neat UPE (0 wt.%) exhibits a smooth, continuous fracture surface typical of an amorphous polymer, with no visible inorganic domains. At 1 wt.% OSP, finely dispersed $CaCO_3$ nanoparticles are embedded within the matrix, indicating good interfacial adhesion and uniform distribution, with an average particle size of ~43.8 nm. At 5 wt.% OSP, the inorganic phase becomes more pronounced, and particle dispersion remains relatively uniform, although partial clustering increases the average particle size to ~108.0 nm. This microstructure favors effective stress transfer and crack deflection, correlating with enhanced mechanical performance. At 9

wt.% OSP, noticeable nanoparticle agglomeration is observed, with average particle size increasing to ~114.4 nm. These clusters act as potential stress concentrators and explain the slight reduction in properties at high loading. FESEM analysis identifies 3–7 wt.% OSP as the optimal dispersion range for composite reinforcement [28,29].

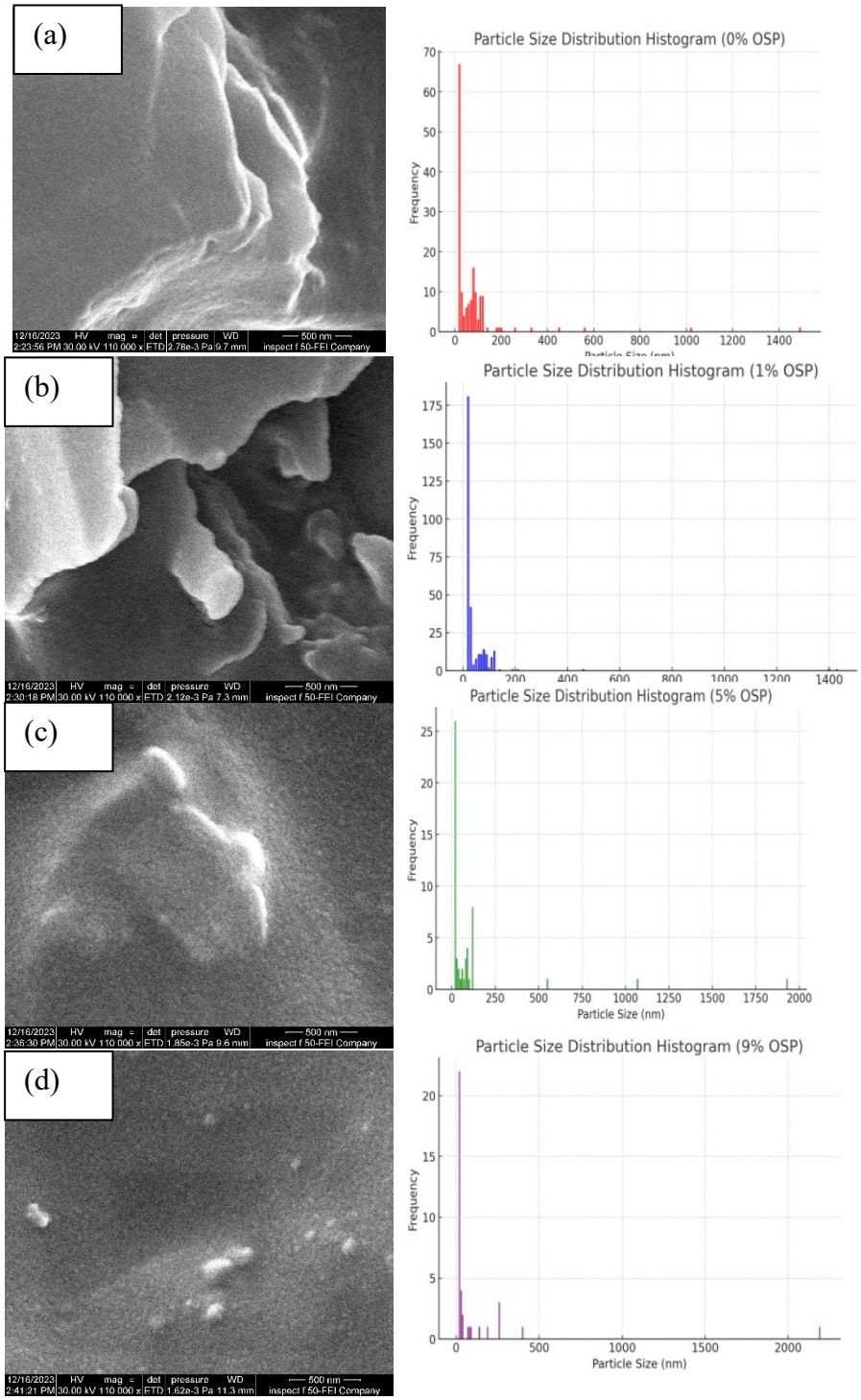

Figure 6 FESEM images of UPE/OSP composites at 0%, 1%, 5%, and 9 wt.% OSP nanofiller loadings

4.5. FTIR analysis

The FTIR spectra of the UPE/OSP composites (Figure 7) display the characteristic absorption bands of unsaturated polyester along with distinct vibrational modes associated with calcite $CaCO_3$. Neat UPE (0 wt.%) shows a strong C=O stretching band at ~1720 cm^{-1}, ester-related C–O and C–O–C vibrations at ~1250 and ~1120 cm^{-1}, and aliphatic C–H stretching bands in the 2950–2850 cm^{-1} region. With the incorporation of OSP, carbonate-related bands progressively emerge and intensify, particularly the asymmetric CO_3^{2-} stretching at ~1420 cm^{-1}, the out-of-plane bending at ~875 cm^{-1}, and the in-plane bending at ~710 cm^{-1}, confirming the presence of calcite $CaCO_3$. The increasing intensity of these bands correlates with higher nanoparticle loading. Importantly, the positions and shapes of UPE characteristic peaks remain unchanged, indicating that $CaCO_3$ acts as a physically dispersed inorganic phase without altering the chemical structure of the polyester matrix. Stronger carbonate features observed at 5–9 wt.% OSP are consistent with increased filler content and enhanced crystallinity identified by XRD analysis [30-33].

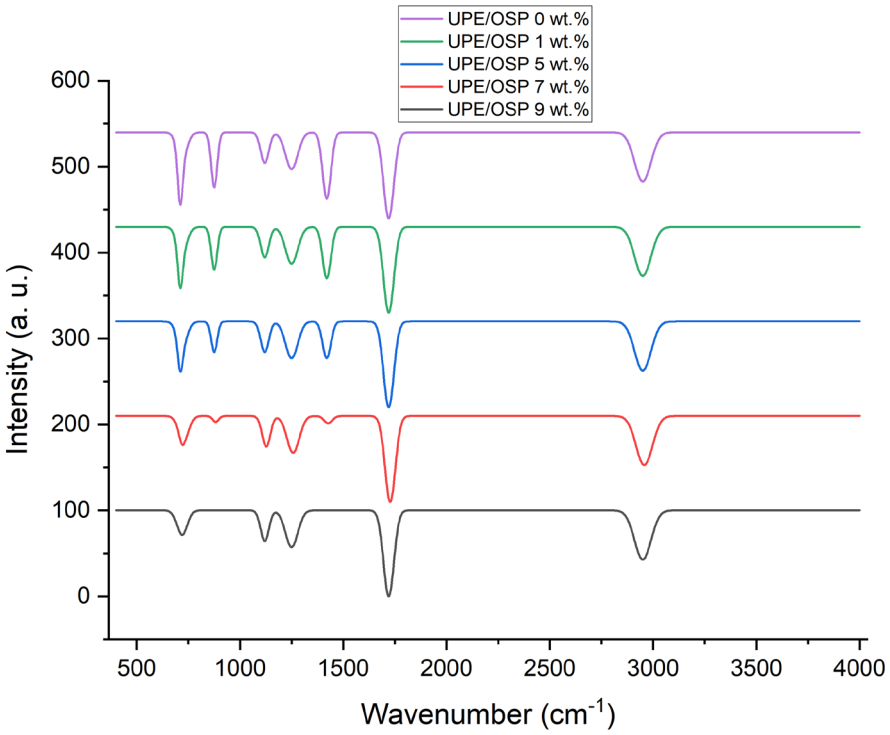

Figure 7 FTIR transmittance spectra of UPE/OSP composites containing 0 to 9 wt.% $CaCO_3$ NPs

4.6. Mechanical properties

4.6.1. Impact strength

Table 9 summarizes the effect of OSP nanoparticle loading on the impact strength of UPE composites, revealing a non-linear response. Neat UPE exhibits an impact strength of 8.74 ± 0.10 kJ/m². A decrease at 1 wt.% OSP (7.92 ± 0.06 kJ/m²) suggests initial stress concentration due to incomplete reinforcement. Impact strength improves at 3 wt.% (8.16 ± 0.05 kJ/m²) and reaches a maximum at 5 wt.% OSP (9.08 ± 0.05 kJ/m²), reflecting optimal nanoparticle dispersion, effective crack deflection, and efficient energy dissipation. Beyond this level, impact resistance declines at 7 and 9 wt.% due to

matrix stiffening and nanoparticle agglomeration. These trends correlate well with FESEM and XRD analyses, confirming 5 wt.% OSP as the optimal loading for enhanced impact performance [34,35].

Table 9 Impact strength (I_s) of UPE/OSP composites at different filler concentrations.

UPE/OSP Conc. (%)	Rep1	Rep2	Rep3	Rep4	Rep5	I_s Mean ± SD (kJ/m²)
0	8.62	8.79	8.88	8.70	8.72	8.74 ± 0.10
1	7.85	7.98	7.90	7.88	7.99	7.92 ± 0.06
3	8.10	8.20	8.18	8.11	8.21	8.16 ± 0.05
5	9.02	9.15	9.11	9.05	9.07	9.08 ± 0.05
7	7.55	7.68	7.59	7.66	7.58	7.61 ± 0.05
9	7.28	7.35	7.30	7.36	7.36	7.33 ± 0.03

4.6.2. Tensile strength

Table 10 summarizes the tensile strength of UPE/OSP composites, reported as mean ± SD, with low deviations (0.03–0.06 MPa) indicating excellent repeatability. Neat UPE exhibits a tensile strength of 7.70 ± 0.05 MPa. Incorporation of 1 wt.% OSP markedly increases tensile strength to 11.79 ± 0.06 MPa, reflecting efficient stress transfer and good nanoparticle dispersion. A gradual increase is observed at 3 wt.% (11.93 ± 0.03 MPa) and 5 wt.% (12.77 ± 0.04 MPa). The maximum tensile strength of 13.90 ± 0.06 MPa occurs at 7 wt.% OSP, corresponding to optimal dispersion and strong interfacial adhesion. A slight decline at 9 wt.% (12.89 ± 0.05 MPa) is attributed to nanoparticle agglomeration. These results identify 7 wt.% OSP as the optimal loading for tensile reinforcement [36, 37].

Table 10 Tensile strength σ_t of UPE/OSP composites at different filler concentrations.

UPE/OSP Conc. (%)	Rep1	Rep2	Rep3	Rep4	Rep5	Tensile Strength σ_t (MPa) (Mean ± SD)
0	7.62	7.70	7.74	7.71	7.72	7.70 ± 0.05 MPa
1	11.70	11.82	11.83	11.76	11.83	11.79 ± 0.06 MPa
3	11.88	11.96	11.94	11.93	11.96	11.93 ± 0.03 MPa
5	12.70	12.80	12.77	12.75	12.81	12.77 ± 0.04 MPa
7	13.82	13.90	13.92	13.89	13.97	13.90 ± 0.06 MPa
9	12.81	12.92	12.89	12.88	12.94	12.89 ± 0.05 MPa

4.6.3. Hardness test

Table 11 illustrates the effect of OSP nanoparticle loading on the Shore D hardness of UPE/OSP composites. Neat UPE exhibits a baseline hardness of 75.0 ± 0.29. Hardness increases steadily with filler addition, reaching 78.5 ± 0.31 at 1 wt.% and 80.2 ± 0.26 at 3 wt.% due to restricted polymer-chain mobility and improved matrix stiffness. Further enhancement is observed at 5 wt.% (82.6 ± 0.31), and the maximum hardness of 85.1 ± 0.27 is achieved at 7 wt.% OSP, reflecting optimal nanoparticle dispersion and effective load transfer. A slight decrease at 9 wt.% (83.4 ± 0.26) indicates the onset of nanoparticle agglomeration and matrix saturation. These results confirm that 5–7 wt.% OSP provides optimal reinforcement for maximizing surface hardness [38,39].

Table 11 Hardness (Shore D) of UPE/OSP composites at different filler concentrations from 0-9 wt.%

UPE/OSP Conc. (%)	Rep1	Rep2	Rep3	Rep4	Rep5	Hardness (Mean ± SD)
0	74.6	75.2	75.3	74.8	75.1	75.0 ± 0.29
1	78.1	78.9	78.6	78.4	78.8	78.5 ± 0.31
3	79.8	80.5	80.4	80.1	80.3	80.2 ± 0.26
5	82.1	82.9	82.7	82.5	82.8	82.6 ± 0.31
7	84.7	85.4	85.2	85.1	85.3	85.1 ± 0.27
9	83.0	83.6	83.5	83.3	83.7	83.4 ± 0.26

4.6.4. Flexural strength

Table 12 summarizes the flexural strength of UPE composites reinforced with 0–9 wt.% OSP nanoparticles. Neat UPE exhibits the lowest flexural strength (60.5 ± 0.1 MPa). The addition of OSP leads to a progressive increase in bending strength, reaching 68.7 ± 0.1 MPa at 1 wt.% and 72.4 ± 0.1 MPa at 3 wt.% due to enhanced stiffness and improved stress transfer. A further increase is observed at 5 wt.% (77.6 ± 0.1 MPa), corresponding to effective filler dispersion and reinforced load-bearing pathways. The maximum flexural strength (81.9 ± 0.1 MPa) occurs at 7 wt.% OSP, indicating optimal reinforcement. A slight decline at 9 wt.% (78.3 ± 0.1 MPa) is attributed to nanoparticle agglomeration and matrix saturation. These results highlight 7 wt.% OSP as the optimal loading for flexural performance [40,41].

Table 12 Mean Values of σ_f vs UPE/OSP composites at different filler concentrations 0-9 wt.%.

UPE/OSP Conc. (%)	Rep1	Rep2	Rep3	Rep4	Rep5	σ_f (MPa) Mean ± SD
0	60.6	60.5	60.5	60.4	60.6	60.5 ± 0.1
1	68.8	68.7	68.6	68.7	68.7	68.7 ± 0.1
3	72.5	72.3	72.4	72.4	72.4	72.4 ± 0.1
5	77.6	77.7	77.6	77.5	77.6	77.6 ± 0.1
7	81.9	82.0	81.9	81.8	81.9	81.9 ± 0.1
9	78.3	78.4	78.2	78.3	78.3	78.3 ± 0.1

4.6.5. Thermal conductivity

Table 13 shows the effect of OSP nanoparticle loading on the thermal conductivity of UPE/OSP composites. Neat UPE exhibits low thermal conductivity (0.345 W/m·°C) due to limited phonon transport in the amorphous polymer matrix. Thermal conductivity increases steadily with OSP addition, reaching 0.368 W/m·°C at 1 wt.%, 0.392 W/m·°C at 3 wt.%, and 0.417 W/m·°C at 5 wt.% as nanoparticles form effective heat-transfer pathways. The maximum value of 0.441 W/m·°C occurs at 7 wt.% OSP, corresponding to optimal filler dispersion and continuous conductive networks. A slight decrease at 9 wt.% (0.429 W/m·°C) is attributed to nanoparticle agglomeration and interfacial scattering. These results identify 5–7 wt.% OSP as the optimal range for enhancing thermal performance [42,43].

Table 13 Thermal Conductivity values (k) of UPE/OSP Composites at Different Nanoparticle Loadings.

UPE/OSP Conc. (%)	Rep1	Rep2	Rep3	Rep4	Rep5	k (W/m.°C) Mean ± SD
0	0.345	0.346	0.344	0.345	0.345	0.345 ± 0.001
1	0.368	0.367	0.369	0.368	0.368	0.368 ± 0.001
3	0.392	0.393	0.392	0.391	0.392	0.392 ± 0.001
5	0.417	0.418	0.417	0.416	0.417	0.417 ± 0.001
7	0.441	0.442	0.441	0.440	0.441	0.441 ± 0.001
9	0.429	0.430	0.428	0.429	0.429	0.429 ± 0.001

4.7. Antibacterial activity

4.7.1. Agar diffusion method: inhibition zone assessment and statistical analysis

The antibacterial performance of UPE/OSP nanocomposites (Figures 14–15, Table 14) shows a statistically significant, concentration-dependent enhancement compared to neat UPE, which exhibits no inhibition against *E. coli* or *S. aureus*. For *E. coli*, inhibition zones increase from 10.05 ± 0.35 mm at 1 wt.% to a maximum of 20.05 ± 0.49 mm at 7 wt.% OSP ($p < 0.001$), followed by a slight decline at 9 wt.% due to nanoparticle agglomeration. *S. aureus* shows smaller but significant inhibition, peaking at 5 wt.% (8.00 ± 0.42 mm, $p < 0.001$). These trends correlate with FESEM and AFM results, confirming that optimal nanoparticle dispersion at 5–7 wt.% maximizes antibacterial efficacy through enhanced nanoparticle–cell interactions [44,45].

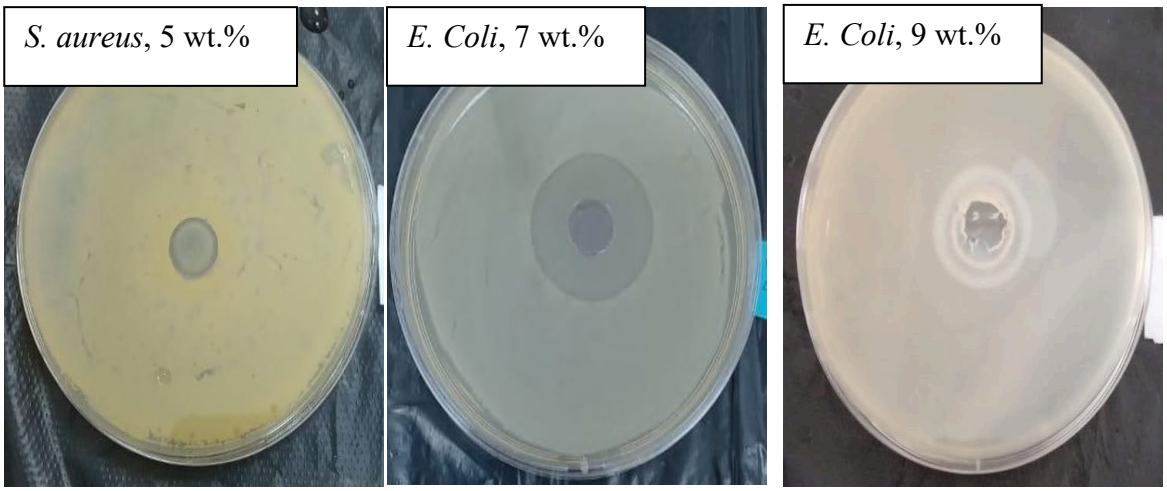

Figure 14. Representative ADM antibacterial plates for UPE/OSP nanocomposites at different NPs loadings

4.7.2. Spread plate method (SPM): assessment and statistical analysis

The antibacterial activity of UPE/OSP nanocomposites is further quantified using the Spread Plate Method (SPM), which measures bacterial survival after direct contact. As shown in Figure 16, *E. coli* CFU counts decreased markedly with increasing OSP content, from 43.0 ± 1.41 CFU at 1 wt.% to complete eradication (0 CFU) at 7 wt.%, confirming strong bactericidal activity. Although slightly reduced at 9 wt.% due to nanoparticle agglomeration, antibacterial performance remained high. In contrast, *S. aureus* exhibited a more moderate response, with optimal suppression at 1–5 wt.% OSP,

reflecting its thicker cell wall structure [46, 47]. All reductions were statistically significant ($p < 0.001$) [48-50]. Together with ADM results, these findings confirm that OSP nanoparticles significantly enhance the antibacterial efficacy of UPE composites, with optimal performance depending on bacterial type [51-54].

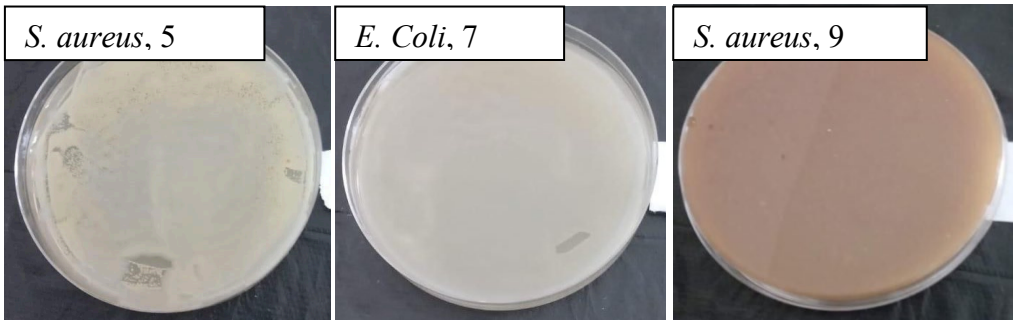

Figure 16 Representative SPM antibacterial plates for UPE/OSP nanocomposites at different NPs loadings

5. CONCLUSIONS

This study demonstrates that the incorporation of oyster/shell-derived $CaCO_3$ nanoparticles (OSP) into unsaturated polyester (UPE) resin significantly enhances the structural, mechanical, thermal, morphological, and antibacterial properties of the resulting composites. Systematic variation of filler loading (1–9 wt.%) revealed effective physicochemical interactions between OSP and the UPE matrix, driven by electrostatic attraction and hydrogen bonding, which promote strong interfacial adhesion and improved structural order. XRD and Williamson–Hall analyses confirmed increased crystallite size and reduced microstrain at moderate filler contents, while AFM and FESEM observations showed optimal dispersion, reduced surface roughness, and uniform morphology at 5–7 wt.% OSP. These structural refinements translated into substantial improvements in tensile, flexural, hardness, impact strength, and thermal conductivity, with peak performance consistently observed in the 5–7 wt.% range. Moreover, OSP imparted pronounced antibacterial activity, particularly against *E. coli*, with complete bacterial elimination at 7 wt.%. Overall, OSP nanoparticles function as multifunctional, sustainable fillers, and the identified optimal loading range offers a practical balance between enhanced performance and minimal agglomeration. These findings highlight the potential of biogenic $CaCO_3$-reinforced UPE composites for advanced structural and hygienic applications.

References

[1] I. Alshalal, H. M. I. Al-Zuhairi, A. A. Abtan, M. Rasheed, M. K. Asmail. J. Mech. Behav. Mater. 32 (2023) 1 https://doi.org/10.1515/jmbm-2022-0280
[2] M. Sellam, M. Rasheed, S. Azizi, T. Saidani. Ceram. Int. 50 (2024) 20917 https://doi.org/10.1016/j.ceramint.2024.03.094
[3] O. Alabdali, S. Shihab, M. Rasheed, T. Rashid. 3rd inter. Scient. conf. alkafeel univ. (ISCKU 2021) (2022) https://doi.org/10.1063/5.0066860
[4] M. Rasheed, O. Alabdali, S. Shihab, A. Rashid, T. Rashid, J. Phys.: Conf. Ser. 1999 (2021) 1 012078 https://doi.org/10.1088/1742-6596/1999/1/012078
[5] N. Assoudi et al. Opt. Quant. Electron. 54 (2022) 9. https://doi.org/10.1007/s11082-022-03927-x
[6] R. Jalal, S. Shihab, M.A. Alhadi, M. Rasheed, J. Phys.: Conf. Ser. 1660 (2020) 012090 https://doi.org/10.1088/1742-6596/1660/1/012090
[7] S. Shihab, M. Rasheed, O. Alabdali, A.A. Abdulrahman, J. Phys.: Conf. Ser. 1879 (2021) 2 022120 https://doi.org/10.1088/1742-6596/1879/2/022120

[8] A. Keziz, M. Heraiz, M. RASHEED, A. Oueslati. Mater Chem. Phys. 325 (2024) 129757 https://doi.org/10.1016/j.matchemphys.2024.129757
[9] D. Kherifi, A. Keziz, M. Rasheed, A. Oueslati. Ceram. Int. 50 (2024) 30175 https://doi.org/10.1016/j.ceramint.2024.05.317
[10] A. Jaber, M. Ismael, T. Rashid, M. A. Sarhan, M. Rasheed, I. M. Sala. Eureka: Phys. Eng. 4 (2023) 29 https://doi.org/10.21303/2461-4262.2023.002770
[11] T. Rashid, M. M. Mokji, M. Rasheed. J. Optics 44 (2024) 55 https://doi.org/10.1007/s12596-024-02080-w
[12] H. K. Aity, E. Dhahri, M. Rasheed. Ceram. Int. 50 (2024) 54666 https://doi.org/10.1016/j.ceramint.2024.10.324
[13] M. Rasheed, S. Shihab, O. Alabdali, A. Rashid, T. Rashid, J. Phys.: Conf. Ser. 1999 (2021) 012077 https://doi.org/10.1088/1742-6596/1999/1/012077
[14] M. Rasheed, M. Nuhad Al-Darraji, S. Shihab, A. Rashid, T. Rashid. J. Phys.: Conf. Ser. 1963 (2021) 012058 https://doi.org/10.1088/1742-6596/1963/1/012058
[15] A. Keziz, M. Heraiz, F. Sahnoune, M. Rasheed, Ceram. Int. 49 (2023) 32989 https://doi.org/10.1016/j.ceramint.2023.07.275
[16] E. Kadri, K. Dhahri, R. Barillé, M. Rasheed. Phase Transi. 94 (2021) 65 https://doi.org/10.1080/01411594.2020.1832224
[17] D. Bouras, M. Rasheed, Opt. Quantum Electron. 54 (2022) 12 https://doi.org/10.1007/s11082-022-04161-1
[18] A. Zubaidi, L.M. Asaad, I. Alshalal, M. Rasheed, J. Mech. Behav. Mater. 32 (2023) 1 https://doi.org/10.1515/jmbm-2022-0302
[19] M. Rasheed et al., J. Phys.: Conf. Ser. 1999 (2021) 012080 https://doi.org/10.1088/1742-6596/1999/1/012080
[20] M. Rasheed, M.N. Al-Darraji, S. Shihab, A. Rashid, T. Rashid, J. Phys.: Conf. Ser. 1963 (2021) 012059. https://doi.org/10.1088/1742-6596/1963/1/012059
[21] M. Enneffatia, M. Rasheed, B. Louati, K. Guidara, S. Shihab, R. Barillé, J. Phys.: Conf. Ser. 1795 (2021) 012050 https://doi.org/10.1088/1742-6596/1795/1/012050
[22] M. Rasheed, O.Y. Mohammed, S. Shihab, A. Al-Adili, J. Phys.: Conf. Ser. 1795 (2021) 012043 https://doi.org/10.1088/1742-6596/1795/1/012043
[23] A.H. Ali, A.S. Jaber, M.T. Yaseen, M. Rasheed, O. Bazighifan, T.A. Nofal, Complexity 2022 (2022) 1 https://doi.org/10.1155/2022/9367638
[24] M. Rasheed, et al., J. Adv. Biotechnol. Exp. Ther. 6 (2023) 495 https://doi.org/10.5455/jabet.2023.d144
[25] M. Rasheed, I. Alshalal, A.A. Ashed, M.A. Sarhan, A.S. Jaber, Indones. J. Electr. Eng. Comput. Sci. 33 (2024) 653 https://doi.org/10.11591/ijeecs.v33.i1.pp653-660
[26] I.M. Mohammed, M. Rasheed, AIP Conf. Proc. 3321 (2025) 020026. https://doi.org/10.1063/5.0289719
[27] F. Boudou, A. Belakredar, A. Berkane, M. Rasheed. Not. Sci. Biol. 17 (2025) 12183 https://doi.org/10.55779/nsb17212183
[28] F. Boudou, et al., Not. Sci. Biol. 17 (2025) 12593 https://doi.org/10.55779/nsb17312593
[29] F. Boudou, A. Guendouzi, A. Belkredar. M. Rasheed, Not. Sci. Biol. 16 (2024) 13837 https://doi.org/10.55779/nsb16211837
[30] R.S. Mahmood et al. J. Mech. Behav. Mater. 34 (2025) 1 https://doi.org/10.1515/jmbm-2025-0040
[31] T. Rashid, M.M. Mokji, M. Rasheed, J. Mech. Behav. Mater. 34 (2025) 77 https://doi.org/10.1515/jmbm-2025-0074
[32] M. Rasheed, M. N. Mohammedali, F. A. Sadiq, M. A. Sarhan, T. Saidani. J. Optics (New Delhi. Print) (2024) https://doi.org/10.1007/s12596-024-01928-5
[33] A.J. Hussein, M.N. Al-Darraji, M. Rasheed, M.A. Sarhan, IOP Conf. Ser.: Earth Environ. Sci. 1262 (2023) 022007 https://doi.org/ 10.1088/1755-1315/1262/2/022007

[34] A.J. Hussein, M.N. Al-Darraji, M. Rasheed, M.A. Sarhan, IOP Conf. Ser.: Earth Environ. Sci. 1262 (2023) 022005 https://doi.org/10.1088/1755-1315/1262/2/022005
[35] T. Saidani, M. Rasheed, I. Alshalal, A.A. Rashed, M.A. Sarhan, R. Barillé, Res. Eng. Struct. Mater. 10 (2024) 743 http://dx.doi.org/10.17515/resm2023.21ma0922rs
[36] M. A. Sarhan, S. Shihab, B. E. Kashem, M. Rasheed, J. Phy.: Conf. Ser., 1879 (2021) 022122 https://doi.org/10.1088/1742-6596/1879/2/022122
[37] M. Rasheed, O. Alabdali, S. Shihab, J. Phy.: Conf. Ser. 1879 (2021) 032120 https://doi.org/10.1088/1742-6596/1879/3/032120
[38] M. Rasheed, R. Barillé, J. Non-Cryst. Solids., 476 (2017) 1 https://doi.org/10.1016/j.jnoncrysol.2017.04.027
[39] M. Rasheed, R. Barillé, Opt. Quantum Electron. 49(2017) 99 https://doi.org/10.1007/s11082-017-1030-7
[40] F. Dkhilalli, S. M. Borchani, M. Rasheed, R. Barille, K. Guidara, M. Megdiche, J. Mater. Sci. Mater. Electron, 29 (2018) 6297 https://doi.org/10.1007/s10854-018-8609-z
[41] A. Boumezoued, K. Guergouri, Régis Barillé, Rechem Djamil, Mourad Zaabat, M. Rasheed, J. Alloys Compd. 791 (2019) 550 https://doi.org/10.1016/j.jallcom.2019.03.251
[42] N. Ben Azaza et al., Opt. Mater. 96 (2019) 109328 https://doi.org/10.1016/j.optmat.2019.109328
[43] Areej Adnan Hateef, Essebti Dhahri, M. Rasheed, Habiba Kadhim, Z. Abbas, N. Hassan, Study of the influence concentration difference of copper in properties of cerium nanopowder, Physics and Chemistry of Solid State 25 (2024) 801 https://doi.org/10.15330/pcss.25.4.801-810
[44] M. Rasheed, SuhaShihab, O. Alabdali, H. H. Hassan, J. Phys. Conf. Ser., 1879 (2021) 032113 https://doi.org/10.1088/1742-6596/1879/3/032113
[45] H. K. Aity, M. Rasheed, E. Dhahri, A. A. Hateef, T. Saidani, Chromium-doped magnesium oxide nanoparticles: dielectric insights and antibacterial potentials, Journal of Materials Science 61 (2026) 6226 https://doi.org/10.1007/s10853-026-12241-w
[46] T. Saidani, S. Mokhtari, M. Rasheed, H. Lahmar, M. Trari, Annealing temperature dependent properties ZnO–TiO_2 bilayer thin films: characteristics and photocatalytic activity, Journal of the Indian Chemical Society 103 (2026) 102499 https://doi.org/10.1016/j.jics.2026.102499
[47] M. RASHEED, A. Khaleefah, Materials Chemistry and Physics, 353 (2026) 132112 https://doi.org/10.1016/j.matchemphys.2026.132112
[48] S. S. Batros, M. Rasheed, H. K. Aity, A. A. Hatef, T. Saidani, Materials Chemistry and Physics 355 (2026) 132243 https://doi.org/10.1016/j.matchemphys.2026.132243
[49] A. Raghdi, M. Heraiz, M. Rasheed, A. Keziz, Investigation of halloysite thermal decomposition through differential thermal analysis (DTA): Mechanism and kinetics assessment, Journal of the Indian Chemical Society, 101 (2024) 101413 https://doi.org/10.1016/j.jics.2024.101413
[50] A. I. A. Ali, M. RASHEED, Effect of changing magnetite percentage on structural and magnetic properties of cobalt ferrite prepared by the sol-gel method, Experimental and Theoretical NANOTECHNOLOGY 10 (2026) 277 https://doi.org/10.56053/10.s.277
[51] A. Khaleefah, M. RASHEED, Sol–gel-derived mullite nanoparticles: Structural and antibacterial insights, Experimental and Theoretical NANOTECHNOLOGY 10 (2026) 289 https://doi.org/10.56053/10.s.289
[52] Z. S. Ahmed, M. RASHEED, H. S. Ahmed, Optimizing NiO nanoparticle properties for antibacterial applications via temperature-driven structural modification, Experimental and Theoretical NANOTECHNOLOGY 10 (2026) 329 https://doi.org/10.56053/10.s.329
[53] Z. S. Ahmed, M. RASHEED, H. S. Ahmed, Enhancing α-Bi_2O_3 nanoparticle crystallinity and antibacterial functionality through controlled calcination, Experimental and Theoretical NANOTECHNOLOGY 10 (2026) 343 https://doi.org/10.56053/10.s.343
[54] A. I. A. Ali, M. RASHEED, Effect of sintering temperature on electrical and structural properties for spinel ferrites prepared by sol-gel method, Experimental and Theoretical NANOTECHNOLOGY 10 (2026) 239 https://doi.org/10.56053/10.s.239

Exp. Theo. NANOTECHNOLOGY 10 (2026) 453-470